Available online at www.sciencedirect.com
ScienceDirect
Catalysis Today 127 (2007) 265–277
CATALYSIS TODAY
www.elsevier.com/locate/cattod

Hydrogen production in solar reactors

Christos C. Agrafiotis [a], Chrysoula Pagkoura [a], Souzana Lorentzou [a], Margaritis Kostoglou [a,b], Athanasios G. Konstandopoulos [a,c,*]

[a] Aerosol & Particle Technology Laboratory, CERTH/CPERI, P.O. Box 361, Thermi, Thessaloniki 57001, Greece
[b] Division of Chemical Technology, Department of Chemistry, Aristotle University, Univ. Box 116, 541 24 Thessaloniki, Greece
[c] Department of Chemical Engineering, Aristotle University, P.O. Box 1517, 54006, Thessaloniki, Greece

Available online 30 July 2007

Abstract

The present work summarizes the recent activities of our laboratory in the field of solar-aided hydrogen production with structured monolithic solar reactors. This reactor concept, ''transferred'' from the well-known automobile exhaust catalytic after-treatment systems, employs ceramic supports optimized to absorb effectively solar radiation and develop sufficiently high temperatures, that are coated with active materials capable to perform/catalyze a variety of ''solar-aided'' reactions for the production of hydrogen such as water splitting or natural gas reforming. Our work evolves in an integrated approach starting from the synthesis of active powders tailored to particular hydrogen production reactions, their deposition upon porous absorbers, testing of relevant properties of merit such as thermomechanical stability and hydrogen yield and finally to the design, operation simulation and performance optimization of structured monolithic solar hydrogen production reactors. This approach, among other things, has culminated to the world's first closed, solar-thermochemical cycle in operation that is capable of continuous hydrogen production employing entirely renewable and abundant energy sources and raw materials – solar energy and water, respectively – without any CO_2 emissions and holds, thus, a significant potential for large-scale, emissions-free hydrogen production, particularly for regions of the world that lack indigenous resources but are endowed with ample solar energy.

Keywords: Solar hydrogen; Monolithic reactors; Water splitting; Steam reforming; Redox materials; Catalytic materials

1. Introduction

The harnessing of the huge energy potential of solar radiation and its effective conversion to chemical energy carriers such as hydrogen is a subject of primary technological interest. There are basically three pathways for producing hydrogen with the aid of solar energy [1]: electrochemical, photochemical and thermochemical. The latter is based on the use of concentrated solar radiation as the energy source for performing high-temperature reactions that produce hydrogen from transformation of various fossil and non-fossil fuels via different routes such as water splitting (to produce hydrogen and oxygen) [1–4], natural gas steam reforming (to produce syngas) [5–8] and natural gas cracking (to produce hydrogen and carbon black nanoparticles) [9–12]. All of these routes involve in some step endothermic reactions that make use of concentrated solar radiation as their energy source of high-temperature process heat.

Obviously, the ideal raw material for hydrogen production is water, due to its abundance, low value and the absence of CO_2 emissions during its dissociation (water splitting) to hydrogen and oxygen. However, although conceptually simple, the single-step thermal dissociation of water (known as water thermolysis):

$$H_2O \rightarrow H_2 + 0.5O_2 \quad (1)$$

is a reaction not favoured thermodynamically; extremely high temperatures (>2200 °C) are required for obtaining some significant dissociation degree [1]; moreover, requires the energy intensive process of high-temperature oxygen–hydrogen separation coupled with expensive membrane technology [13] and therefore is considered of little chance for technical and economical viability in the near future [4]. The current state-of-the-art of solar chemistry for water splitting and hydrogen production is focused on the so-called redox pair cycles. These are two-step processes, based on redox materials that can

* Corresponding author.
E-mail address: agk@cperi.certh.gr (A.G. Konstandopoulos).

0920-5861/$ – see front matter © 2007 Elsevier B.V. All rights reserved.
doi:10.1016/j.cattod.2007.06.039

Nomenclature

c_i	gas phase concentration of species i
c_{1w}	vapor concentration close to the wall
c_{pi}	molar specific heat capacity of species i
c_{pw}	specific heat capacity of the material of the monolith
E_{lo}	activation energy of water splitting reaction
E_{reg}	activation energy of regeneration reaction
f_i	molar flow rate of species i
ΔH_{lo}	heat of water splitting reaction
ΔH_{reg}	heat of regeneration reaction
k_{lo}	rate constant of water splitting reaction
$k_{lo,o}$	frequency factor of water splitting reaction
k_{reg}	rate constant of regeneration reaction
$k_{reg,o}$	frequency factor of regeneration reaction
k_D	mass transfer coefficient in the channel
k_H	heat transfer coefficient in the channel
L	length of the monolith channel
N	number of discretization intervals
P	pressure
Q	solar heating rate per channel
R	universal gas constant
t	time
T	gas temperature
T_w	wall temperature
w	wall thickness
y	fractional surface coverage
Y	average fractional coverage of the monolith
z	coordinate along the monolith

Greek letters

α	size of the side of the monolith channel
ρ_s	density of the material of the monolith
Ψ	storage capacity of the wall

act as effective water splitters at lower temperatures [1–4]. According to this idea, in the first step (water splitting) the activated redox reagent (usually the reduced state of a metal oxide) is oxidized by taking oxygen from water and producing hydrogen via reaction (2) below. During the second step the oxidized state of the reagent is reduced, to be used again (regeneration), delivering some of the oxygen of its lattice according to reaction (3):

$$MO_{red} + H_2O(g) \rightarrow MO_{ox} + H_2(g) \quad (2)$$

$$MO_{ox} \rightarrow MO_{red} + \tfrac{1}{2}O_2 \quad (3)$$

The disadvantage is that a two-step process is required, consisting of a water splitting and a regeneration (oxygen release) step. The advantage is the production of pure hydrogen and the removal of oxygen in separate steps, avoiding the need for high-temperature separation and the chance of explosive mixtures formation.

The redox materials that have been evaluated consist of oxide pairs of multivalent metals such as Fe_3O_4/FeO, Mn_3O_4/MnO – the most representative of which can be considered the Fe_3O_4/FeO system [14] – systems of metal oxide/metal (e.g. ZnO/Zn) [15] and their combinations, e.g. doped ferrites such as $(A,B)Fe_2O_4$ with elements A and B being bivalent metal cations such as Mn, Ni or Zn [16]. Reaction (2) is slightly exothermic whereas reaction (3) is highly endothermic. For example for the system $Mn_{0.5}Zn_{0.5}Fe_2O_4$ a thermodynamic evaluation provided enthalpies of +300 kJ/mol for the O_2 releasing step and between −35 and −68 kJ/mol for the water splitting step [16]. Therefore, water splitting is taking place at temperatures below 900 K while the reduction of the metal oxide, takes place at much higher temperatures. The concept has been proven experimentally, however the regeneration temperatures are still high imposing a barrier towards integration of a two-step water splitting process with a concentrating solar system. For full exploitation of the potential of such cycles, there is a need for materials with high water-splitting activity and regenerability at moderate temperatures, with long-term stability and no properties' degradation over extended cyclic operation under concentrated solar irradiation.

Therefore, at least for a transition period, hydrogen supply at a competitive cost can only be achieved from hydrocarbons—essentially natural gas (whose principal component is methane) using well-known commercial processes like steam reforming where methane and steam are converted to syngas according to reaction (4):

$$CH_4 + H_2O(g) \Leftrightarrow 3H_2 + CO, \qquad \Delta H_{298K} = 206\,kJ/mol \quad (4)$$

In the conventional process, natural gas is fed together with steam to the reformer, where reacts over a catalyst at temperatures between 800 and 1000 °C. In the solar process, it is possible to provide all necessary heat by solar energy [8]. Current state-of-the-art catalytic systems for natural gas steam-reforming are based either on highly expensive precious metals or on systems of significantly lower cost based on Ni-metal supported on mixed oxides of Ca–Al [17] or Mg–Al [18] of the spinels and hexa-aluminates structures (e.g. $MgAl_2O_4$ or $CaAl_6O_7$, respectively). The mixed oxide supports are traditionally synthesized by co-firing of the corresponding oxides at high temperatures (>1600 °C) for extended periods [19] or from wet chemistry routes that also involve sintering of precipitated powders (even though at lower temperatures). This firing is followed by a second calcination step at 500–700 °C under H_2 flow to reduce NiO to "active" Ni. Nevertheless, the use of natural gas as a chemical feedstock and as a fuel in the current hydrogen production processes induces emissions of large quantities of carbon dioxide.

Alternatively, thermal cracking of methane to gaseous hydrogen and carbon black particles according to reaction scheme (5) below, is another promising pathway, towards a more sustainable production of hydrogen, due to carbon sequestration before fuel usage:

$$CH_4 \rightarrow C(s) + 2H_2, \qquad \Delta H_{298K} = 75\,kJ/mol \quad (5)$$

As in the previous cases, high temperatures are required to obtain high methane-to-hydrogen conversion rates and high quality carbon black.

Large-scale concentration of solar energy is mainly accomplished with three kinds of optical configuration systems using parabolic reflectors, namely trough, tower and dish systems. These systems have been proven to be technically feasible in large-scale (MW) pilot and commercial Solar Thermal Power Plants (STPP) aimed at the production of electricity in which a heat transfer fluid (air, water, sodium or molten salt) is solar-heated and further used in traditional energy cycles (Rankine, Brayton or Stirling) appear as a highly viable alternative to fulfill the world's enormous expectation of clean electrical energy. Together with the advancement and commercialization of such STPP the innovative technology of solar volumetric air receiver systems is already advancing at a fast pace. Volumetric receivers consist of high-porosity material structures such as wire meshes, ceramic foams or honeycomb structures that are irradiated by concentrated solar radiation and are used to transfer this radiation to a gaseous heat transfer medium [20,21]. Gas is driven through the absorber parallel to the direction of the incoming radiation and is heated by convection. Since the heat transfer surface per unit of incident solar radiation is increased compared to a tube absorber design, higher flux densities can be transferred without reaching the temperature limit of the absorber material. For example the absorbance of silicon carbide (SiC) due to its naturally black color, coupled with its high thermal conductivity enables the collection of solar heat and effective heating of the reactant gases inside the honeycomb channels—it has already been demonstrated that SiC monoliths can act as collectors of solar heat and achieve temperatures in excess of 1100 °C [22,23].

On the other hand, such porous ceramic structures like monolithic honeycombs and foams are used for several decades in the automotive exhaust after-treatment applications for the performance of high-temperature reactions employing both gaseous and particulate reactants (CO/CO_2, HCs, NOx and soot particulates). Ceramic multi-channelled monolithic honeycomb reactors stem from the heart of ''traditional'' Chemical Engineering and offer an attractive alternative to packed beds when dealing with gaseous reactants at high temperatures; their advantages include thin walls, high geometric surface area and therefore good gas–solid contact, low pressure drop, good mass transfer performance and ease of product separation [24,25]. These can be combined with special material properties such as absorptivity, thermal shock resistance and mechanical strength to couple the collection and exploitation of solar energy with efficient reactor concepts. Solar-thermochemical applications, although not as far developed as solar thermal electricity generation, employ the same solar concentrating technologies but instead of a heat transfer medium, the concentrated solar radiation is focused on a receiver/reactor where chemical reactions are performed. Provided that catalytic or redox materials effective and durable at these temperature levels can be synthesized, a variety of solar chemistry reactions can be performed with such materials immobilized upon the porous support walls of solar receivers/reactors, avoiding the needs of continuous powder feeding and collection from the reactor. Therefore, this reactor geometry can be successfully transferred to solar applications, creating new opportunities for the ''solar hydrogen'' chemistry.

Current engineering challenges in the field of ''solar chemistry'' include development of advanced solar concentrators, synthesis of active materials for solar chemistry reactions (catalysts, redox materials) and design and operation of novel receiver/reactor systems capable to collect effectively the concentrated solar radiation and at the same time to perform in an efficient and elegant manner the high-temperature reactions mentioned above. In order to scale-up solar reactors, parameters such as the reactor volume and the loading with the redox/catalyst coating required have to be optimized, taking into account the solar flux and the resulting temperature distribution, the heat transfer characteristics, the reaction rates and transient phenomena due to reactor operation at alternating solar flux conditions. An important point that has to be quantified is the influence of reaction enthalpies on the operational behavior. For instance, during the exothermic water splitting process, due to inadequate heat dissipation, hot spots might arise within the reactor, that can cause reaction (3) above to take place simultaneously with reaction (2) and introduce undesirable oxygen in the product stream.

During the last 6 years, our laboratory has developed a significant activity in the field of solar chemistry, by developing advanced materials and technologies for solar hydrogen production systems with emphasis on structured monolithic solar reactors. Particular successful examples of such materials and technologies that can be fully integrated in Solar Thermal Power Plants include:

- pilot-scale synthesis of active redox and catalytic materials that can achieve production of hydrogen at relatively low temperatures;
- tailored deposition of such powders on porous supports;
- assessment of monolithic ceramic honeycombs used as volumetric solar thermal reactors/receivers;
- design of filtering devices for solar-produced carbon black nanoparticles;
- design, simulation and performance optimization of structured monolithic solar hydrogen production reactors including mathematical modeling of transport processes and chemical reactions, operation simulation and optimization.

Selected experimental results of these activities have been reported in several publications [23,26–31]. The present work reviews the developments so far and updates them with further experimental results as well as presents for the first time modeling of such systems and operation simulation results to account for the effects of both reaction kinetics and enthalpies on the reactor characteristics, highlighting the current research efforts focused on long-term material stability and scale-up of solar reactors.

2. Material development

Synthesis routes currently pursued in our laboratory are based on aerosol and combustion processes. The rationale for this choice is that both these kinds of routes share the common characteristics of very short synthesis times and extremely high cooling rates and therefore are capable of producing particles with high defects concentration; in addition they can take place within reactors of controlled reaction atmosphere; for instance controlled oxygen partial pressure can ''tune'' the products' oxygen vacancies concentration for the case of water-splitting materials, whereas an inert or reducing environment can aid the reduction of NiO to metal Ni for the case of steam reforming. Further common advantages are potential for nano-particle synthesis, ease for precisely controlled doping, no requirement of sintering at high temperatures and amenability to scale-up. Last but not least, both these methods are extremely flexible: a wide variety of material compositions can be synthesized with the same experimental configuration.

With this perspective, redox water-splitting materials based on doped iron oxides and steam-reforming catalytic systems based on Ni-metal supported on mixed oxides such as Ca–Al and Mg–Al were synthesized in our laboratory via ''non-traditional' combustion and aerosol routes: self-propagating high-temperature synthesis (SHS), and aerosol spray pyrolysis (ASP). The synthesis details have been reported previously [27,29], therefore only the general reaction concepts are reported below. For comparison purposes, materials of similar compositions were also synthesized via the ''traditional'' solid-state synthesis (SSS) route by co-firing of the component oxides under air and comparatively evaluated.

2.1. SHS (or combustion synthesis)

SHS (or combustion synthesis) of the targeted materials is based on the heat released from the exothermic reaction of a metal powder (''fuel'', e.g. either Fe or Al/Mg for the water-splitting redox materials and the steam-reforming catalytic materials, respectively) with oxygen (''oxidizer'') in the presence of the corresponding metal oxides (Fe_2O_3, NiO, MnO, ZnO for the former case and Al_2O_3, MgO for the latter). The dopant metal oxides are used not only to control the final products' stoichiometry, but also as a ''thermal ballast/moderator'' to control the synthesis temperature. For instance a typical reaction scheme for mixed iron oxides synthesis is the following (where A and B denote the dopant bivalent metals, either Mn, Zn or Ni):

$$2k\mathrm{Fe} + (1-k)\mathrm{Fe_2O_3} + x\mathrm{AO} + y\mathrm{BO} + (1.5k)\mathrm{O_2} \rightarrow (\mathrm{A}_x\mathrm{B}_y)\mathrm{Fe}_z\mathrm{O_4} \quad (6)$$

Typical reaction schemes for the synthesis of $MgAl_2O_4$ supports for the Ni catalysts for the steam-reforming case are the following:

$$2k\mathrm{Al} + (1-k)\mathrm{Al_2O_3} + \mathrm{MgO} + 3k\mathrm{O_2} \rightarrow \mathrm{MgAl_2O_4} \quad (7)$$

$$k\mathrm{Mg} + (1-k)\mathrm{MgO} + y\mathrm{Al_2O_3} + \tfrac{k}{2}\mathrm{O_2} \rightarrow \mathrm{MgAl_2O_4} \quad (8)$$

The synthesis of the spinel substrate was followed by its impregnation into a $Ni(NO_3)_2$ solution, subsequent calcination to remove the nitrate ions and synthesize the NiO phase and finally a second calcination under reducing atmosphere (500–700 °C under H_2) to reduce the NiO formed into Ni. In order to avoid the two post-synthesis calcination steps and produce in situ Ni-metal supported upon the desirable mixed oxide, the following SHS reaction schemes were also investigated:

$$x\mathrm{NiO} + 2k\mathrm{Al} + (1-k)\mathrm{Al_2O_3} + y\mathrm{MgO} + 3k\mathrm{O_2} \rightarrow x\mathrm{Ni} + \mathrm{MgAl_2O_4} \quad (9)$$

$$x\mathrm{NiO} + k\mathrm{Mg} + (1-k)\mathrm{MgO} + \mathrm{Al_2O_3} + \tfrac{k}{2}\mathrm{O_2} \rightarrow x\mathrm{Ni} + \mathrm{MgAl_2O_4} \quad (10)$$

2.2. Aerosol spray pyrolysis

Aerosol spray pyrolysis employs the atomization of a solution of the metal precursor salts in a spray of fine droplets that is subsequently passed through a hot-wall reactor where it transforms within a very short time to ultra-fine, spherical particles [32]. The ASP experiments took place with aqueous solutions of nitrates (Fe, Zn, Mn and Ni for the mixed iron oxide-based redox materials and Al, Mg and Ni for the steam-reforming catalytic materials, respectively) employing two kinds of aqueous solutions: ''plain'' and citric acid-additized. The effect of the atmosphere (air or inert N_2) on the final products was also investigated. The solutions were atomized with the aid of an in-house atomizer (droplet mean diameter ≈2 μm) and the droplets formed pass through a tubular reactor heated between 350 and 1070 °C, where the evaporation of the solvent and the reaction between the precursors take place. Typical reaction schemes for the two cases are like the following:

$$2\mathrm{Fe(NO_3)_3} + x\mathrm{A(NO_3)_2} + y\mathrm{B(NO_3)_2} \rightarrow (\mathrm{A}_x\mathrm{B}_{1-x})\mathrm{Fe_2O_4} + \mathrm{N_2} + \mathrm{O_2} \quad (11)$$

$$2\mathrm{Al(NO_3)_3} + \mathrm{Mg(NO_3)_2} + x\mathrm{Ni(NO_3)_2} \rightarrow x\mathrm{NiO}\cdot\mathrm{MgAl_2O_4} + \mathrm{N_2} + \mathrm{O_2} \quad (12)$$

2.3. Products' comparison

The phase composition of typical mixed iron oxides synthesized via the various routes is compared in Fig. 1a. Depending on the synthesis route, the product can be from single-phase doped spinel $(A_xB_y)Fe_zO_4$ either very well or much less crystallized (SSS, ASP, respectively) or a mixture of doped wustite ($A_xB_yFe_{1-x-y}O$) and spinel (SHS). Typical SEM pictures of products from the two routes are shown in Fig. 1b and c. Products from SHS form dense, sintered grains (Fig. 1b) whereas ASP produced powders are inherently spherical (Fig. 1c) and very fine (of the order of few hundreds of nanometers); their size depends on the solution properties, the atomization process, the synthesis temperature and the residence time in the synthesis reactor.

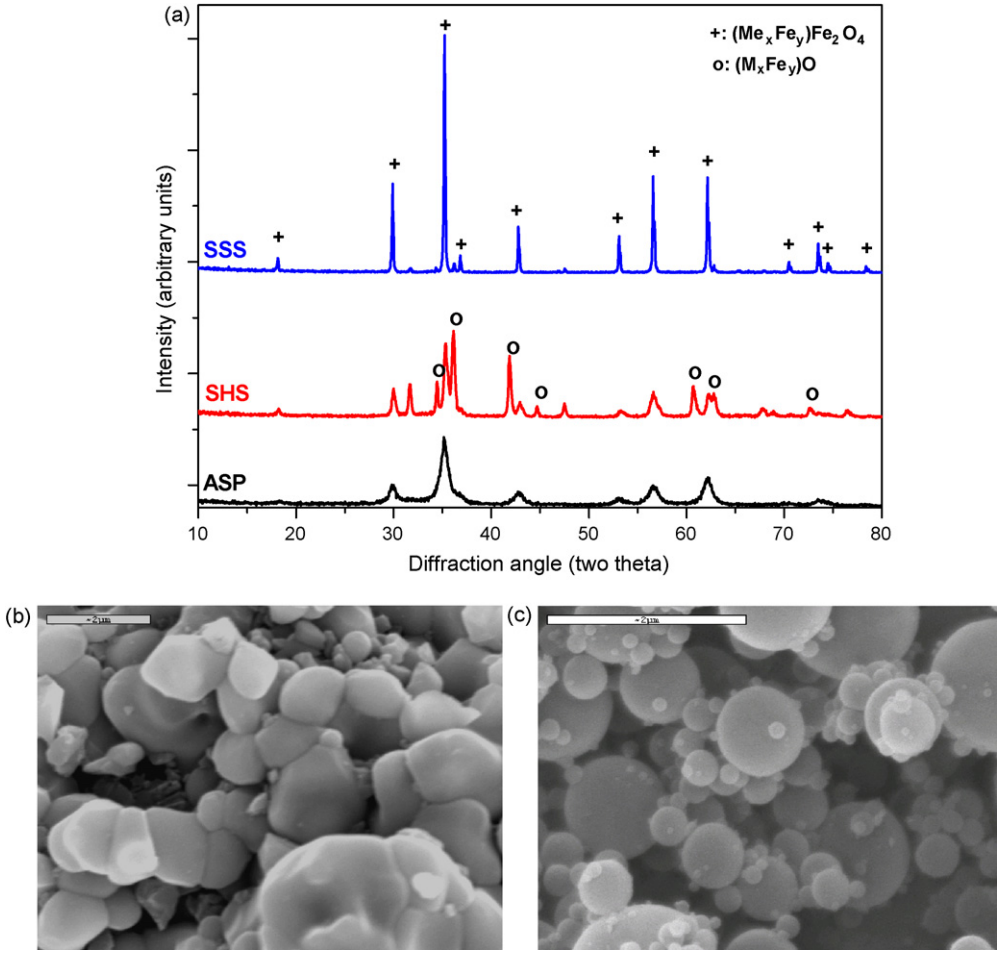

Fig. 1. Phase composition and morphology comparison among iron-oxide-based redox products synthesized from the various routes: (a) XRD comparison; SEM pictures: (b) SHS, (c) ASP.

For the case of steam-reforming catalytic materials, all the SHS reactions employed (with either Al or Mg used as fuel) were capable of producing mixed oxide substrates of the desirable phases (such as $MgAl_2O_4$) after proper adjustment of reactants stoichiometry (e.g. of value *k*: fuel/moderator ratio), due to the very high temperatures developed during the reactions (1400–1500 °C). Typical products from the various routes are compared versus a ''reference'' $MgAl_2O_4$ spinel synthesized by solid-state synthesis (co-firing of the constituent oxides) in Fig. 2. In addition, with proper adjustment of reactants stoichiometry, reaction schemes (9) and (10) were capable of producing Ni-metal supported on mixed $MgAl_2O_4$ spinel supports, as it can be seen from the respective XRD spectrum of a product of reaction (9) shown in Fig. 2. Even though quantities of the oxides Al_2O_3 and MgO exist in the products, the existence of metallic Ni strongly suggests that, with proper further ''fine-tuning'' of the reactants stoichiometry, these reaction schemes have the potential to synthesize directly Ni-spinel systems, avoiding the calcination and reduction steps. The main difference between Al-derived (reactions (7) and (9)) and Mg-derived products (reactions (8) and (10)) is that the former were highly sintered whereas the latter were in all cases loose powders with smaller mean diameter and higher surface area.

ASP-synthesized materials, irrespective of the aqueous solution used, the atmosphere employed or the synthesis temperature, are nano-crystalline as suggested from the low intensity and the high width of the XRD peaks (Fig. 2). The main product phases are Ni–Al spinel ($NiAl_2O_4$) and MgO.

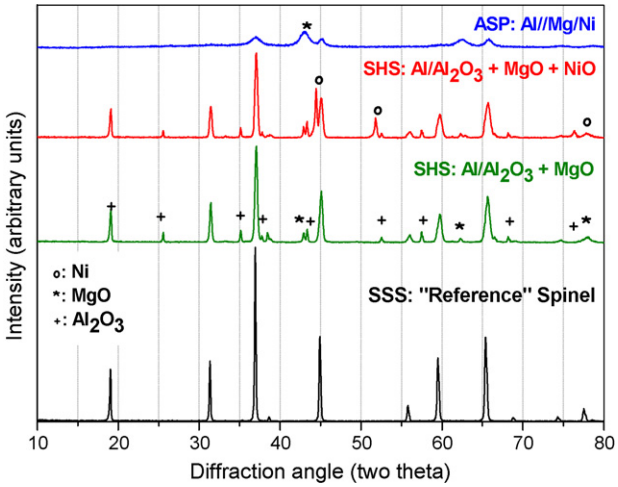

Fig. 2. Phase composition comparison among steam-reforming catalytic systems synthesized from the various routes.

SEM photographs of the synthesized powders have shown that the particles are always spherical, with a high percentage being of submicron size whereas the EDS elemental microanalysis showed that the particles are homogeneous containing all three metal components, Al, Mg and Ni.

2.4. Hydrogen production

The first ''screening'' of the synthesized material compositions with respect to water splitting activity was performed in a laboratory unit described in detail previously [26] and subsequently in a scaled-up testing rig version consisting of a 20-mm-diameter quartz glass tubular reactor enclosed within a high-temperature programmable furnace capable of reaching temperatures of 1500 °C. A bed of the redox-material powder to be tested was placed in the middle of the reactor and subsequently heated under inert atmosphere (nitrogen) to the water-splitting testing temperature. When this temperature was reached, steam was introduced to the reactor. The effluent, after passing through a water trap, was diverted to the analysis rig, consisting of an MS detector, a CO and a CO_2 analyzer. Each water-splitting experiment lasted until hydrogen could not be further detected in the effluent stream; thereafter the steam flow was switched off, the reactor was cooled down and the redox materials were collected for ex situ characterization. The quantities of unconverted water and of produced hydrogen were calculated based on the areas of the corresponding MS peaks.

These experiments have shown that several systems from all the synthesis routes were able to split water and generate hydrogen as the only product, at temperatures as low as 800 °C and could be repeatedly regenerated under inert atmospheres at temperatures below 1200 °C [27]. The ''best'' products from each synthesis route are compared with respect to water-to-hydrogen conversion and total hydrogen yield in Fig. 3a and b, respectively. Both SHS and ASP materials exhibited very high water conversions (amount of water converted/total amount of injected water) at 800 °C—57 and 81%, respectively. Overall the ASP materials exhibited both the highest water conversion and hydrogen yield.

The same test rig was employed for the methane steam-reforming catalytic tests. The gas mixture used in this case was CH_4/H_2O: 1/2.5, with He as a carrier gas. Before the catalytic evaluation, reduction of the catalyst at 750 °C under H_2 took place. The (%) CH_4 conversion achieved from different ASP products, all synthesized at 900 °C, during a thermo-programmed cycle, is shown in Fig. 4. The catalytic activity of the products varies: products synthesized under air, are capable of CH_4 conversion, whereas those synthesized under N_2, were found inactive. The product derived from a citric acid solution achieves the highest conversion, which, though, did not remain stable during the catalytic test, probably due to surface area loss caused by further sintering.

3. Coating of porous supports

As already mentioned, the materials eventually have to be coated on ceramic honeycomb substrates capable to absorb concentrated solar radiation. Therefore, in analogy with the procedure followed for the automobile catalytic converters, ''washcoating'' of the support with the redox material has to take place. Washcoating involves preparation of a stable slurry of the coating powder, impregnation of the support, drying and subsequent firing in the temperature range 550–700 °C to achieve strong adhesion of the coating on the support. However, in the case of the specific water-splitting redox materials, this adhesion firing cannot take place under air or oxidizing

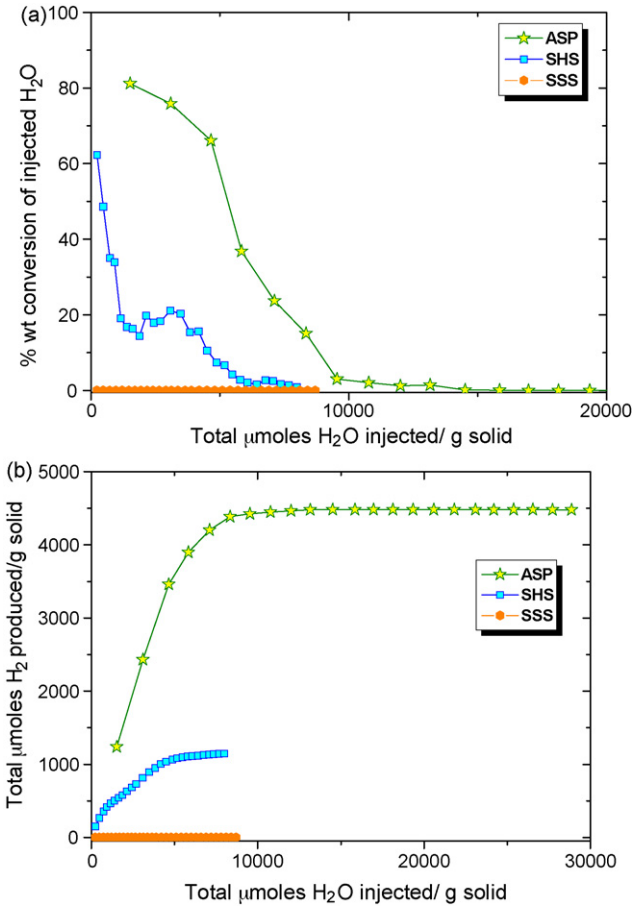

Fig. 3. Comparison of ''best'' redox powders from each synthesis route with respect to: (a) water conversion and (b) total hydrogen yield.

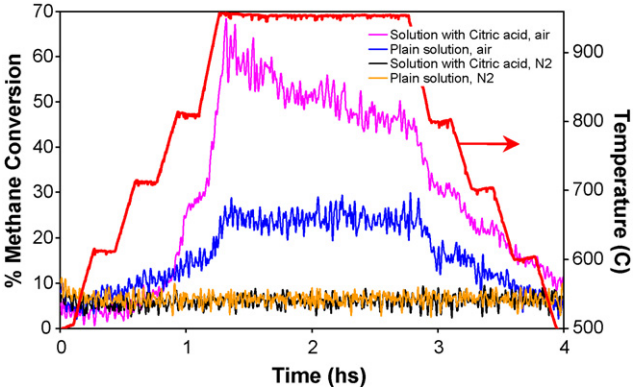

Fig. 4. CH_4 steam-reforming conversion to hydrogen achieved from ASP products.

atmosphere, since this will cause oxidation of the ''reduced'' state of the metal oxide and thus inability to act as water-splitter—the use of inert atmosphere is therefore imperative.

A preliminary ''simulation'' of the adhesion firing process was performed in the water-splitting test rig. Powders were placed in the quartz reactor, heated under nitrogen up to 800 °C where they remained for 2 h, cooled at ambient temperature again under nitrogen, removed and characterized via XRD to detect the phase changes taking place. In parallel, the as-synthesized materials were calcined in a sintering furnace under air atmosphere for 5 h at the same water-splitting testing temperatures, to ensure their ''saturation'' with oxygen and determine the maximum ''oxygen storage capacity'' as a function of material composition and temperature. The XRD spectra of two typical Zn–Fe–O materials synthesized by SHS and ASP that have demonstrated the highest water conversion, are shown in Fig. 3. In these figures, the XRD spectra of each as-synthesized material are compared with the spectra of the same material after reaching the water-splitting temperature of 800 °C under N_2 atmosphere (but before introducing steam), after water splitting at 800 °C until its saturation with oxygen and after calcination in air atmosphere at 800 °C for 5 h; in addition the visual appearance of the materials after each stage is compared to ''reference'' hematite (Fe_2O_3, red-brown) and magnetite (Fe_3O_4, black) materials.

It can be observed that the SHS as-synthesized material is a mixture of doped wustite $(Zn_xFe_y)O$, ZnO and spinel $(Zn_xFe_y)Fe_2O_4$ phases that is transformed almost completely to wustite and ZnO after ''adhesion firing'', to spinel, ZnO and a small percentage of trivalent iron oxide (Fe_2O_3) after completion of the water-splitting step and to spinel and a small amount of Fe_2O_3 after calcination in air. On the contrary, the ''as-synthesized ASP material is a low-crystallized spinel phase that is transformed to a mixture of spinel, wustite and metallic iron during adhesion firing at 800 °C under N_2; these are the phases present just before the introduction of steam. The material after water splitting is transformed to single-phase spinel, whereas after calcination in air becomes trivalent iron oxide (Fe_2O_3).

The presence of trivalent iron oxide after calcination in air in both families of redox materials (SHS and ASP) renders them ''red-brown'' in color. On the contrary the black color of both materials after water splitting indicates that whatever trivalent iron ions are formed, still remain in the spinel crystal structure; the materials during water splitting take oxygen from water but are not transformed irreversibly to the trivalent oxide but to a

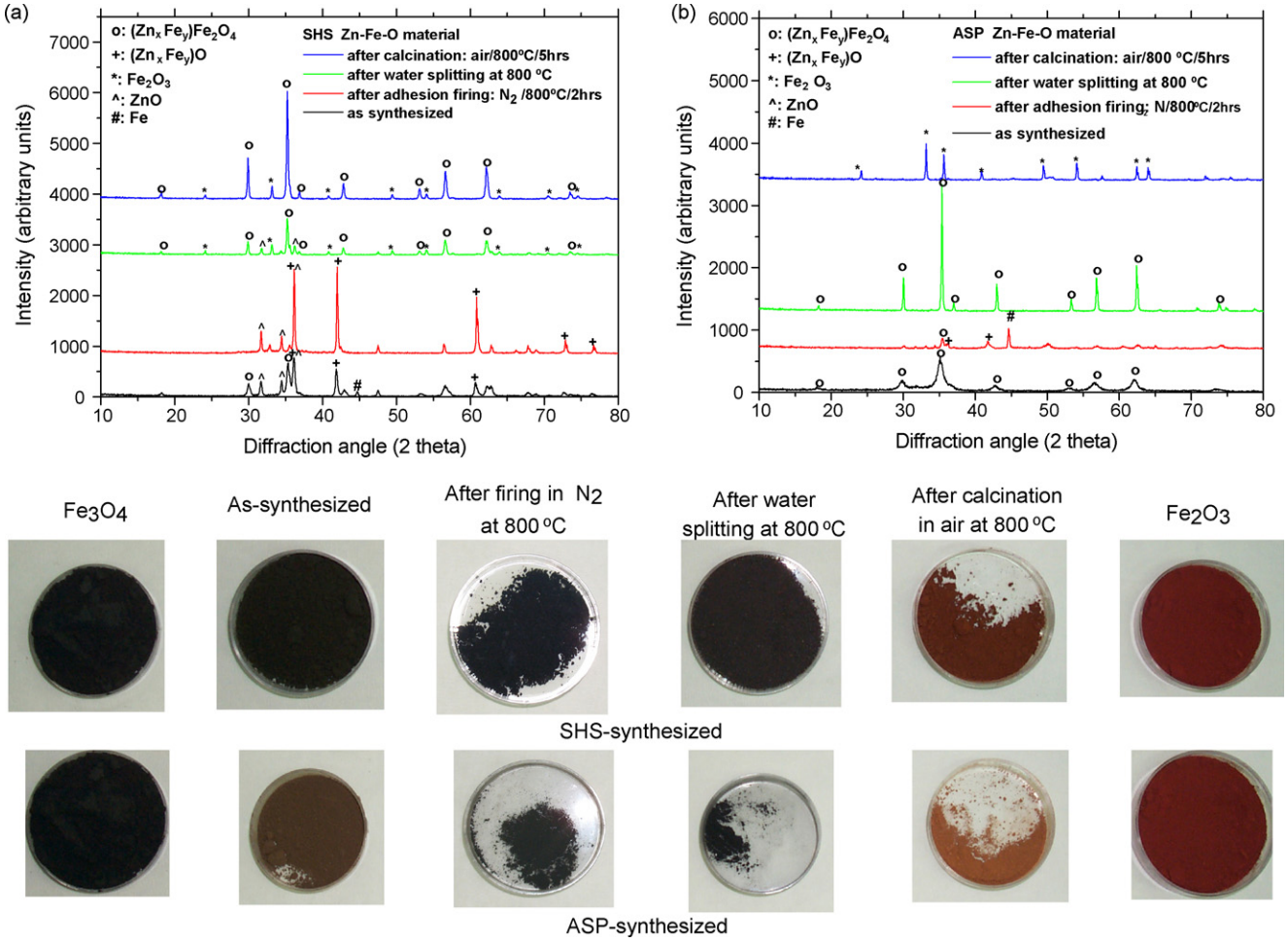

Fig. 5. (a and b) XRD (top row) and color (bottom rows) comparison of SHS- and ASP-synthesized Zn–Fe–O redox materials after the various processing steps. From left to right: ''reference'' magnetite (Fe_3O_4, black), as-synthesized materials, materials after calcination at 800 °C under N_2, materials after water splitting at 800 °C, materials after calcination in air at 800 °C, ''reference'' hematite (Fe_2O_3, red-brown).

spinel phase which is much more easily reduced to the bivalent oxides and is therefore is easily capable for cyclic operation.

The next step involved coating of SiC honeycombs and foams with the synthesized materials via the ''washcoating'' technique employed for the coating of automotive catalysts, in which the porous supports are impregnated in a slurry of the coating powder [24]. For the water-splitting case, extruded multi-channel honeycombs with cell density of 90 channels per square inch (cpsi) from recrystallized and silicon-metal-infiltrated (siliconized) silicon carbide (abbreviations reSiC and siSiC, respectively), manufactured by Stobbe Tech Ceramics, Denmark, were evaluated with respect to pore structure and thermomechanical properties both in the ''as-manufactured'' state as well as after prolonged operation as solar thermal collectors under solar irradiation in order to understand the phenomena that take place under exposure to solar irradiation, increase the lifetime of exposed receiver elements, and tailor their properties to those of the active coating materials. The detailed comparison results have already been reported [23]; therefore only details of the coating process are given here. Slurries of the SHS-synthesized powders were prepared with solids content varying between 50 and 80 wt% and stabilized with the aid of suitable dispersants. Small test-size siSiC and reSiC honeycomb pieces (Ø 25 mm, 90 cpsi, length 15–50 mm) were impregnated in the powder slurries, dried and fired at 800 °C under nitrogen atmosphere to ensure efficient adhesion of the redox powder upon the substrate while retaining its oxygen-deficient structure. To improve on long-term stability of the coating/support assembly and to prevent any reactions between the redox powder and the support material, an intermediate coating layer was applied on the monolith before that of the redox material, to offer structural and chemical stabilization. Fully yttria stabilized zirconia (YSZ, ZrO_2 containing 8 mol%/13.27 wt% of Y_2O_3) was used for that intermediate layer since it has been reported that addition of zirconia to a ferrite redox powder has helped in suppressing sintering of the ferrite and enhanced its reactivity [33]. Characteristic SEM photographs of such a monolith are shown in Fig. 5a and b from where it can be clearly seen that the ZrO_2 layer interpolates between the monolith and the redox material and isolates them. Different ''families'' and ''generations'' of redox pair materials coated on such small-scale honeycombs were evaluated in a solar test reactor that was built and operated at the German Aerospace Center DLR, Cologne, Germany. Several solar campaigns have proved beyond any doubt the proposed concept: not only the reactor was capable for producing hydrogen from steam at the expense of solar energy alone, but multi-cyclic operation (water splitting and redox-material regeneration) at the temperature range 800–1200 °C was successfully demonstrated several times and for several of the redox materials synthesized [28,30]. Coated honeycombs have demonstrated cyclic water-splitting/regeneration operation for 52 cycles, providing an almost constant amount of hydrogen and showing only minor evidence of coating quality deterioration [28]. Current efforts are targeted in optimizing the oxide coating loading and determining the kinetics of the water-splitting and regeneration reactions.

For the steam-reforming case, SHS-synthesized materials (20% Ni supported on $MgAl_2O_4$) were applied as coatings upon 20 ppi (pores per inch) SiC foams provided by DLR, Stuttgart, Germany, with a similar procedure (washcoating, adhesion firing). Typical photographs of the ''first generation'' of such coated foams after the various processing steps (washcoating, activation by heating under 5% H_2/N_2 at 750 °C for 2 h and ''aging'' by heating under 5% H_2/N_2 at 1000 °C for 10 h) are shown in Fig. 6c–f. The ''fresh'' coated foam just after adhesion firing (Fig. 6d, blue-green color) exhibited an absorptivity of ∼80%—a value considered low for solar applications.

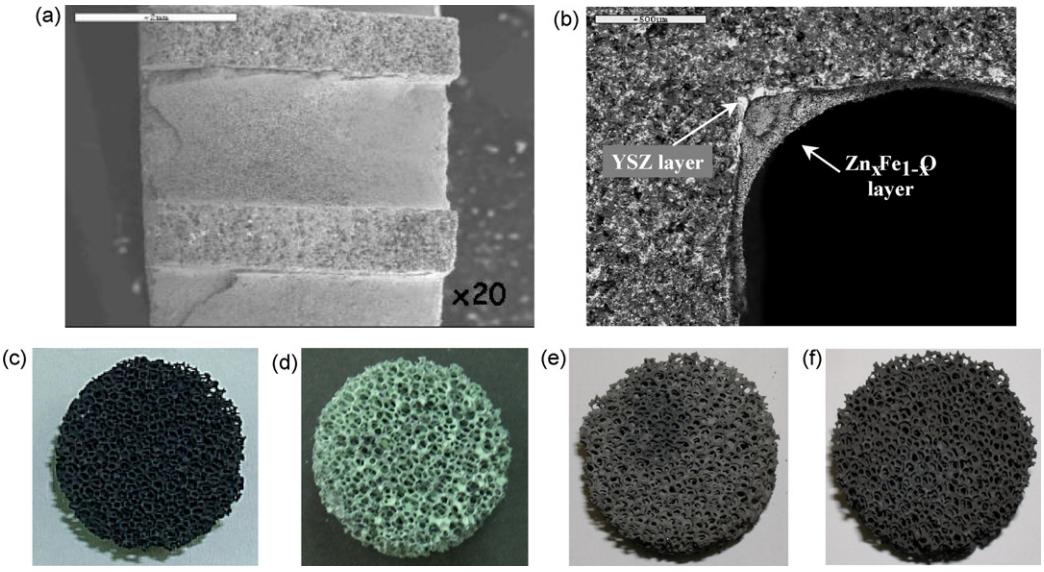

Fig. 6. Top row: SiC honeycombs for solar water splitting. SEM photographs of a monolith impregnated in a zirconia slurry and in a $Zn_xFe_{1-x}O$ slurry: (a) ''top'' view of coated channels, (b) ''front'' view magnification of the support/coating interphase. Bottom row: SiC foams for solar steam reforming after various process stages: (c) un-coated foam, (d) same foam coated with a 20% Ni-catalyst, (e) same foam after activation (reduction at 750 °C in 5%H_2/N_2 at 750 °C/2 h) exhibiting absorptivity 93%, (f) same foam after aging (in 5%H_2/N_2 at 1000 °C/10 h) exhibiting absorptivity 96%.

However, after each subsequent reduction step, its absorptivity increased first to 93% after activation (Fig. 6e) and eventually to 96% after aging (Fig. 6f) – the highest absorptivity among its competitor materials of higher cost – obviously due to the black color of the Ni-metal occurring after reduction. Additional methane and biogas steam-reforming catalytic tests performed on the coated systems (not reported here for reasons of brevity) have demonstrated satisfactory catalytic activity of the coated systems for both reactions.

4. Modeling and simulation of monolithic solar hydrogen reactors

In parallel to the experimental work, a mathematical model for the description of the cyclic water-splitting/regeneration process was formulated to describe the water-splitting process towards the production of hydrogen, inside a honeycomb monolithic reactor under the influx of solar radiation on its front face. Although the modeling of catalytic monoliths used by the automotive industry for environmental purposes has been studied extensively [34], the solar radiation boundary condition at the reactor phase sets-up a new mathematical problem, not studied previously. The model includes the basic mass, momentum and energy transport processes as well as the heterogeneous surface reactions of water vapor with the redox coating on the channels of the reactor. Emphasis is placed on identifying the design factors of the monolithic reactor affecting its thermal response during its cyclic operation between water-splitting and coating regeneration cycles. These factors have to be taken into account to prevent the regeneration reaction to take place simultaneously with the water-splitting one and to overall optimize the reactor design and the operational cycle.

4.1. Assumptions

It is assumed that the behavior of the coated monoliths can be illustrated by one representative channel (one dimensional problem). The main assumptions of the model are the following: (i) uniform mass flow distribution within the monolith. (ii) Laminar flow within the monolith channel. Enhanced heat and mass transfer between gas phase and solid phase close to the converter inlet due to boundary layer build-up. (iii) Axial heat radiation and axial gas phase conduction are negligible compared to the heat convection. (iv) The coated honeycomb is well insulated (adiabatic). (v) The redox material does not deactivate. (vi) All mechanisms involved in the conversion of gas species (adsorption, desorption, pore diffusion, reaction) are lumped into the overall reaction rate expressions.

4.2. Reaction scheme

The mathematical model is developed on the channel basis (and not on the monolith basis as is the usual case in literature [35,36]). The unit module includes a channel and the half thickness of the wall around it. To get a single formulation for both loading and regeneration stages the model is developed assumed four species in the gas phase: H_2O ($i = 1$), inert gas N_2, ($i = 2$), H_2 ($i = 3$) and O_2 ($i = 4$). The following reactions are assumed to occur on the redox-material-coated wall of the monolith:

- water splitting

$$M + H_2O \rightarrow MO + H_2 \tag{13}$$

- coating regeneration

$$MO \rightarrow M + \tfrac{1}{2}O_2 \tag{14}$$

The model is developed in terms of molar flow rates f_i (per channel) of species since the molar fraction of the reactive species can be quite large and the dilute limit approximation (typically employed in the simulation of automotive catalytic converters [37]) is not valid. The rates of the above reactions were assumed to be:

$$R_{\text{splitting}} = \Psi k_{\text{lo}} c_1 (1 - y) \tag{15}$$

$$R_{\text{regeneration}} = \Psi k_{\text{reg}} y \tag{16}$$

where Ψ is the storage capacity of the wall (in terms of equivalent vapor moles per monolith area = intrinsic redox-material storage capacity × loading), y the fractional surface coverage and c_1 is the gas phase hydrogen concentration. The reaction rate constants k_{lo}, k_{reg} have Arrhenius type temperature dependence.

$$k_{\text{lo}} = k_{\text{lo,o}}\, e^{-E_{\text{lo}}/RT} \tag{17}$$

$$k_{\text{reg}} = k_{\text{reg,o}}\, e^{-E_{\text{reg}}/RT} \tag{18}$$

4.3. Mass and heat balances

From the assumptions above, the equations describing the monolith dynamics are the following (where α is the side size of the square channel, L the length of monolith and w the thickness of the wall of the monolith):

4.3.1. Gas phase

Species conservation:

(i) H_2O:

$$\frac{df_1}{dz} = -4\alpha k_{\text{D}} (c_1 - c_{1\text{w}}) \tag{19}$$

The flux of the wall must be equal to the reaction rate:

$$k_{\text{D}} (c_1 - c_{1\text{w}}) = R_{\text{lo}} = k_{\text{lo}} c_{1\text{w}} (1 - y) \tag{20}$$

Eliminating $c_{1\text{w}}$ from the above equation and substituting in (19) leads to:

$$\frac{df_1}{dz} = -4\alpha R_{\text{lo}} = \frac{k_{\text{lo}} k_{\text{D}} c_1 \Psi (1 - y)}{k_{\text{D}} + k_{\text{lo}} \Psi (1 - y)} \tag{21}$$

(ii) Inert gas:

$$\frac{df_2}{dz} = 0 \tag{22}$$

(iii) H_2:

$$\frac{\mathrm{d}f_3}{\mathrm{d}z} = 4\alpha R_{\mathrm{lo}} \tag{23}$$

(iv) O_2:

$$\frac{\mathrm{d}f_4}{\mathrm{d}z} = 2\alpha R_{\mathrm{reg}} \tag{24}$$

Energy conservation:

$$\left(\sum_{i=1}^{4} f_i c_{pi}\right)\frac{\mathrm{d}T}{\mathrm{d}z} = 4\alpha k_{\mathrm{h}}(T_{\mathrm{w}} - T) \tag{25}$$

4.3.2. Solid phase

Surface coverage evolution:

$$\Psi\frac{\mathrm{d}y}{\mathrm{d}t} = R_{\mathrm{lo}} - R_{\mathrm{reg}} \tag{26}$$

Energy conservation:

$$2\rho_{\mathrm{s}} c_{p\mathrm{w}} w\alpha\frac{\partial T_{\mathrm{w}}}{\partial t} = 2\lambda w\alpha\left(\frac{\partial^2 T}{\partial z^2}\right) + 4\alpha k_{\mathrm{h}}(T - T_{\mathrm{w}}) + 4\alpha(\Delta H_{\mathrm{lo}} R_{\mathrm{lo}} + \Delta H_{\mathrm{reg}} R_{\mathrm{reg}}) \tag{27}$$

The concentrations in the gas phase are computed as:

$$c_i = \frac{f_i}{\sum_{i=1}^{n} f_i}\frac{P}{RT} \tag{28}$$

In the above equations c_{pi} is the molar specific heat capacity of the gaseous species i, $c_{p\mathrm{w}}$ the specific heat capacity of the monolith's material, λ,ρ_{s} the conductivity and density of the same material, ΔH the reaction enthalpies, k_{h} the channel to wall heat transfer coefficient and k_{D} the channel to wall mass transfer coefficient.

4.4. Boundary/initial conditions

The boundary and initial conditions for the coated monolith are as follows (where $Q(t)$ is the solar power adsorbed by the monolith per channel):

$$f_i(0,t) = f_{i\mathrm{o}}(t) \tag{29}$$

$$T(0,t) = T_{\mathrm{o}}(t) \tag{30}$$

$$-\lambda\frac{\partial T_{\mathrm{w}}}{\partial z} = \frac{Q(t)}{2w\alpha} \text{ at } z = 0 \tag{31}$$

$$\frac{\partial T_{\mathrm{w}}}{\partial z} = 0 \text{ at } z = L \tag{32}$$

Initial condition:

$$T_{\mathrm{w}}(x,0) = T_{\mathrm{wo}} \tag{33}$$

4.5. Method for numerical solution

The numerical solution of the above system of equations is not trivial due to the character of the solutions. Depending of the problem parameters quite sharp temperature and surface coverage fronts can be appeared. The numerical technique employed here is based on finite analytic techniques for the gas phase and finite volumes for the solid and is capable to capture correctly the fronts and in additional to conserve exactly the total mass and total enthalpy. The channel length is cut in N equal pieces using the discretization points $z_i = i/N$ ($i = 0, 1, 2, \ldots, N$). The gas temperature T_i refers to the point z_i whereas the wall temperature $T_{\mathrm{w}i}$ refers to mean temperature of the interval (z_{i-1}, z_i) (Fig. 7). The main assumption is that: $y(z) = y_i$ and $T_{\mathrm{w}}(z) = T_{\mathrm{w}i}$ at the i wall interval. Based on this assumption, a system of 2 N ordinary differential equations for $T_{\mathrm{w}i}$ and y_i is derived. This system is stiff and it cannot be integrated with explicit techniques so an integrator for stiff systems is employed [38].

4.6. Simulation results and implications

In order to present the capabilities of the computational tool developed here some typical values for the kinetic constants and activation energies of the reactions are chosen and simulations are performed for the basic set of parameters shown in Table 1. The parameters regarding the geometric features of the monolith are typical for commercial monoliths. The kinetic parameters are typical values estimated from the experiments performed in the laboratory. The monolith material parameters are those of silicon carbide. Typical values for the flow rate of the inert gas, the rate of adsorbed solar energy and the inlet gas temperature (similar to those used in the pilot plant) have been assumed. The only operational parameter value used that is irrelevant to actual pilot plant development is the flow rate of the water vapor. A small flow rate of vapor is assumed (about 9% molar fraction). For this molar flow rate the heat of reaction is too small to influence the monolith temperature, so the coupling between the thermal and the chemical kinetic problem is approximately one-way. This one-way influence of the

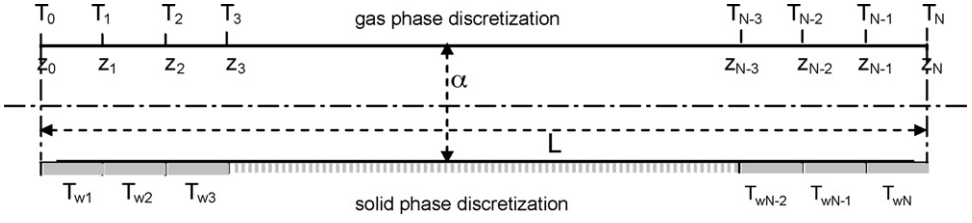

Fig. 7. Discretization scheme along the channel.

Table 1
Parameter values used in the simulation

W (m)	0.0008
L (cm)	20
α (m)	0.002
Ψ (mol/m^2)	0.1
$k_{lo,o}$ (m^3/mol/s)	35
$k_{reg,o}$ (s^{-1})	10^6
E_{lo} (J/mol)	10^5
E_{reg} (J/mol)	240,000
ρ_s (kg/m^3)	2000
c_{pw} (J/K/kg)	1000
λ (W/m/K)	100
Q (J/s)	1
f_{1o} (mol/s)	3×10^{-6}
f_{2o} (mol/s)	3×10^{-5}
T_o (°C)	150

temperature evolution on the chemical kinetic problem is of interest here.

The thermal response of the system was studied first. Starting from an initial state of the monolith at 25 °C and switching on the gas flow and the solar heating, the evolution of the gas temperature leaving the monolith is shown in Fig. 8a. At t = 3000 s the solar heat flux is shut-off completely for 1200 s (case A), 600 s (case B) or reduced to its half for 1200 s (case C). There are two mechanisms for the transfer of the heat given by the solar source along the monolith: convective transfer using the gas flow and transfer via the solid phase conduction. For the case presented here the thermal capacity of the gas is very small so the local equilibration between gas and solid temperature is very fast. The large thermal conductivity leads to a uniform profile of the temperature in the monolith and to an exponential heat up. The monolith's wall temperature profiles corresponding to case A of Fig. 8a are shown in Fig. 8b. The profiles are smooth (relatively small temperature variation) having the maximum temperature at the inlet of the monolith during the heating period and at the outlet during the cooling period.

In order to assess the influence of the thermal conductivity of the monolith on its thermal response, the outlet gas temperature for the conditions of case A and several values of thermal conductivity is shown in Fig. 9a. In general, the smaller the thermal conductivity, the faster the thermal response of the monolith. As the conductivity decreases the gas heating curve is no more exponential but exhibits an induction period followed by a very steep increase and reaches a steady state temperature. The primary heat transfer mechanism is no more the conduction through the solid but the gas-phase transfer (convection). It is clearly shown in Fig. 9a that for the same time after shutting-off the solar heat source the decrease of the gas temperature can be several hundred degrees higher in the case of small conductivity. Although small solid conductivity leads to faster thermal response and from a cursory view should be desirable, for the present type of applications, it has the very important disadvantage of leading to very steep temperature profiles with temperature gradients which may cause material failures. The gas temperature profiles corresponding to the case λ = 1 W/m/K of Fig. 9a, at several time instants, are shown in Fig. 9b. The

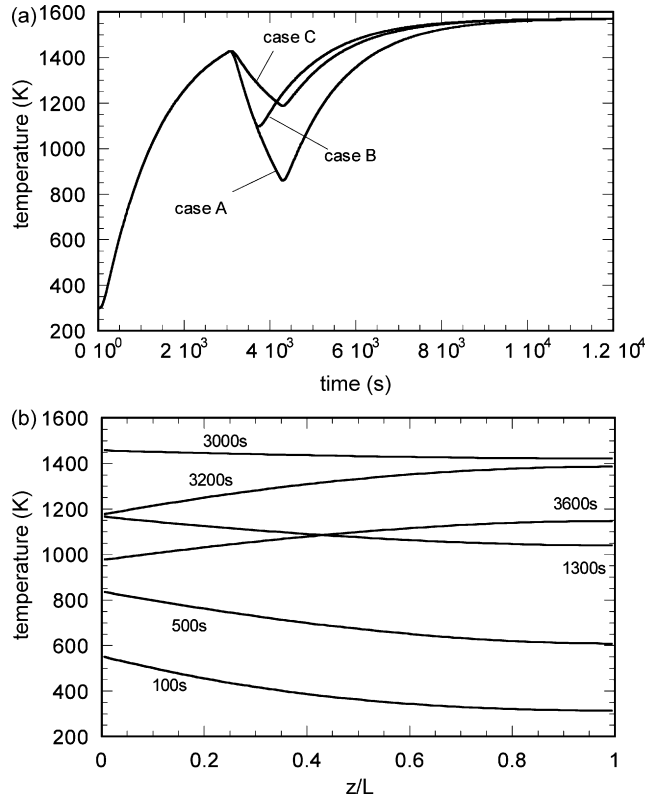

Fig. 8. (a) Evolution of gas temperature at the outlet of the monolith; (b) snapshots of the wall temperature profile corresponding to case A.

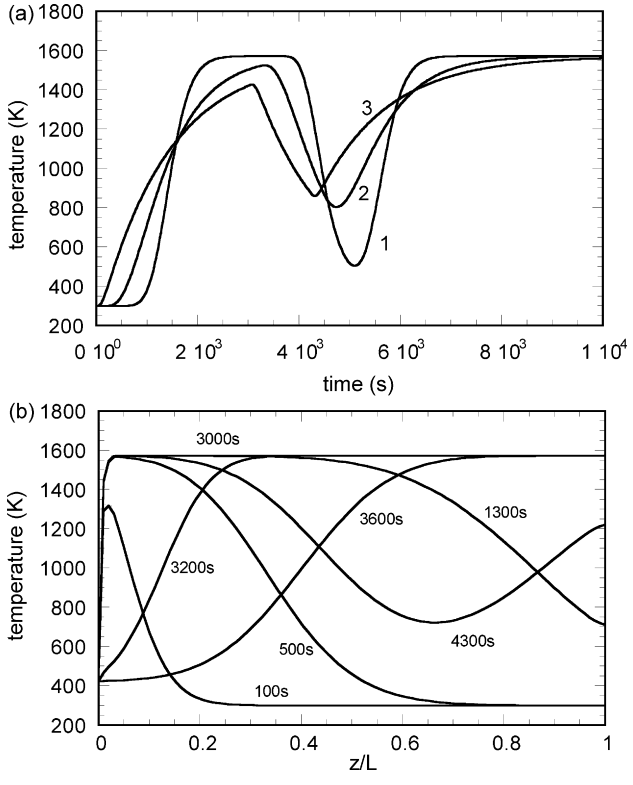

Fig. 9. (a) Evolution of gas temperature at the outlet of the monolith, Case A, (1) λ = 1 W/m/K (2) λ = 10 W/m/K (3) λ = 100 W/m/K; (b) snapshots of the gas temperature profile corresponding to the Case A with λ = 1 W/m/K.

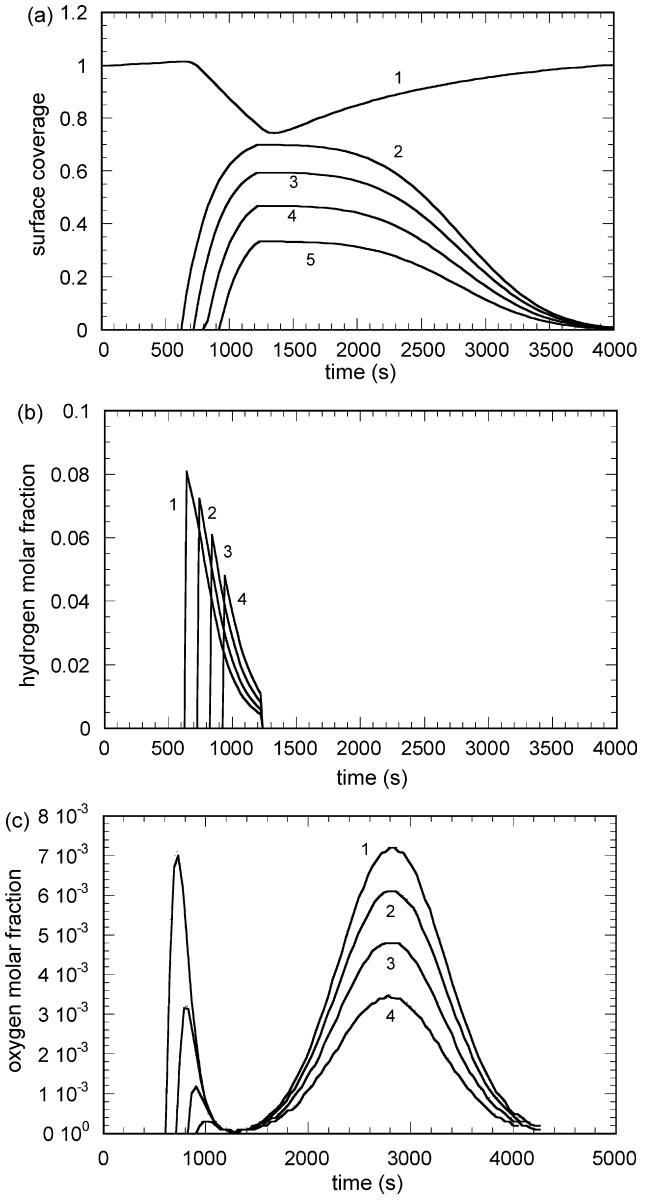

Fig. 10. (a) average surface coverage Y for several values of time delay between pause of heating and starting of vapor flow. (1) Dimensionless temperature; (2) Y for $\delta t = 0$; (3) Y for $\delta t = 100$ s; (4) Y for $\delta t = 200$ s; (5) Y for $\delta t = 300$ s. (b) Hydrogen and (c) oxygen, molar fraction in outlet gas for several values of time delay between pause of heating and starting of vapor flow.

heating and the cooling processes proceed through a temperature front of finite thickness moving from the heated side to the other one. The existence of this front can explain the gas temperature evolution shown in Fig. 8b. As has been already noticed the gas temperature is very close to the solid temperature due to small thermal capacity of the gas. Only at the inlet region gas and solid have appreciably different temperatures. As the conductivity decreases the thickness of the temperature front becomes smaller. As conductivity increases the thickness of the front increases until to become equal to the monolith size and disappear progressively leading to a uniform temperature profile. It can be shown that for channels with large aspect ratio as the present one, radiation can be handled as an additional temperature-dependent conductivity. For high-temperature values like these encountered in the particular application, the radiation-induced apparent conductivity can be larger than the intrinsic one so the main effect of radiation would be the increase of the apparent conductivity of the monolith.

The effect of the temperature management on the overall reaction kinetics of the system was studied next. The system is considered at steady state having the solar source turned on and an inert gas feed. Then the source is shut off at time $t = 600$ s and after some time δt the inert feed is switched to one containing water vapor (with 9% molar fraction). The return to the inert feed is made at $t = 1200$ s. The effect of the time delay δt on the evolution of the adsorption state of the coating and the composition of the outlet stream is shown in Fig. 10a–c. In Fig. 10a the evolution of the average fractional coverage $Y = 1/L \int_0^L y \, dx$ of the active sites of the monolith is presented. After switch-on of the vapor feed the redox material is loaded with oxygen with a rate decreasing with time as both temperature and driving force $(1 - y)$ decrease. After $t = 1200$ s loading stops due to absence of water vapor in the feed and the temperature is too small for regeneration so the surface coverage remains constant for a period. As the temperature increases, regeneration sets on leading to complete removal of the oxygen from the redox material. Obviously the smaller is the time delay δt, the higher is the maximum coverage achieved (being proportional to the efficiency of the process).

The evolution of the molar fraction of hydrogen in the outlet stream is presented in Fig. 10b. Initially (at $t = 600 + \delta t$) a large amount of the water in the feed is transformed to hydrogen. Progressively the hydrogen concentration decreases due to the temperature and driving force $(1 - y)$ decrease. Again it is obvious that the efficiency of the process is higher as the value of δt is smaller (vapor feed starts at higher temperature). On the other hand, if the redox material becomes exposed at high temperature, the simultaneous regeneration reaction is inevitable as it is obvious from the evolution of the oxygen molar fraction in the outlet stream presented in Fig. 10c. As δt increases the degree of overlap between the two sub-processes decrease until their independent occurrence which is required for the efficient operation of the overall process.

5. Conclusions

Material synthesis routes and chemical reactor concepts and technologies having already demonstrated their success and established in other areas, can be effectively ‘‘transferred’’ to solar chemistry applications for the realization of solar hydrogen production, taking of course into account the peculiarities of high-temperature cyclic operation of solar reactors.

Aerosol and combustion synthesis processes are currently pursued in our laboratory to exploit on the one hand their short synthesis times and high cooling rates that lead to materials with high defects concentration and on the other hand their flexibility for synthesizing a wide variety of material compositions with the same experimental apparatus. Several iron-oxide-based redox pair systems targeted to solar-aided

water splitting and $MgAl_2O_4$-supported-Ni targeted to natural gas solar-aided steam reforming have been synthesized via both technologies, characterized and comparatively evaluated. Advantages of the particular synthesis routes have been demonstrated by tests on properties of merit on final products: these materials have achieved superior performance (hydrogen yield, regeneration capability) compared to conventionally synthesized materials of the same composition.

Coating techniques were successfully employed for the preparation of multi-layer, multi-functional coatings on porous ceramic supports, meeting the thermomechanical operation demands of solar reactors and providing long-term stability of the coating/support assembly. These combined efforts have culminated to the development of a honeycomb solar reactor for the continuous production of solar hydrogen via water splitting; the reactor is currently producing hydrogen exclusively at the expense of solar energy being the world's first closed, solar-thermochemical cycle in operation, capable of continuous hydrogen production.

In parallel, a mathematical model formulated to describe the water-splitting process inside such a reactor under the influx of solar radiation on its front face, has been developed. Reactor operation simulations have demonstrated the important role of the thermal conductivity of the reactor material in distributing not only the incoming solar energy but also the heat of the water-splitting reaction along its length. These factors have to be taken into account to prevent the regeneration reaction to take place simultaneously with the water-splitting one and to over-all optimize the reactor design and the operational cycle for an efficient process scale-up.

Acknowledgements

The authors would like to thank the European Commission for partial funding of this work within the Projects ''SOLAIR: Advanced solar volumetric air receiver for commercial solar tower power plants'' (ERK-CT1999-00021), ''HYDROSOL: Catalytic monolith reactor for hydrogen generation from solar water splitting'' (ENK6-CT-2002-00629), ''SOLREF: Solar steam reforming of methane rich gas for synthesis gas production'' (FP6-2002-Energy-1, 502829), HYDROSOL-II: ''Solar Hydrogen via Water Splitting in Advanced Monolithic Reactors for Future Solar Power Plants'' (FP6-2004-Energy-3, 020030) and ''SOLHYCARB: Hydrogen from Solar Thermal Energy: High Temperature Solar Chemical Reactor for Co-production of Hydrogen and Carbon Black from Natural Gas Cracking'' (FP6-2002-Energy-1, 019770) and their partners in these projects.

References

[1] A. Steinfeld, Sol. Energy 78 (2005) 603.
[2] Y. Tamaura, A. Steinfeld, P. Kuhn, K. Ehrensberger, Energy 20 (1995) 325.
[3] T. Kodama, Prog. Energy Combust. Sci. 29 (2003) 567.
[4] C. Perkins, A.W. Weimer, Int. J. Hydrogen Energy 29 (2004) 1587.
[5] V.I. Anikeev, A.S. Bobrin, J. Ortner, S. Schmidt, K.H. Funken, N.A. Kuzin, Sol. Energy 63 (1998) 97.
[6] D. Hirsch, M. Epstein, A. Steinfeld, Int. J. Hydrogen Energy 26 (2001) 1023.
[7] T. Kodama, T. Shimizu, T. Satoh, M. Nakata, K.-I. Shimizu, Sol. Energy 73 (2002) 363.
[8] S. Möller, D. Kaucic, C. Sattler, J. Sol. Energy Eng. Trans. ASME 128 (2006) 16.
[9] P.V. Zedtwitz, J. Petrasch, D. Trommer, A. Steinfeld, Sol. Energy 80 (2006) 1321.
[10] J.K. Dahl, K.J. Buechler, A.W. Weimer, A. Lewandowski, C. Bingham, Int. J. Hydrogen Energy 29 (2004) 725.
[11] S. Abanade, G. Flamant, Int. J. Hydrogen Energy 30 (2005) 843.
[12] S. Abanades, G. Flamant, Sol. Energy 80 (2006) 1611.
[13] A. Kogan, Int. J. Hydrogen Energy 25 (2000) 1043.
[14] A. Steinfeld, S. Sanders, R. Palumbo, Sol. Energy 65 (1999) 43.
[15] A. Steinfeld, Int. J. Hydrogen Energy 27 (2002) 611.
[16] Y. Tamaura, M. Kojima, T. Sano, Y. Ueda, N. Hasegawa, M. Tsuji, Int. J. Hydrogen Energy 23 (1998) 1185.
[17] A.M. Gadalla, B. Bower, Chem. Eng. Sci. 43 (1988) 3049.
[18] A.A. Lemonidou, I.A. Vasalos, Appl. Catal. A 54 (1989) 119.
[19] D. Domanski, G. Urretavizcaya, F.J. Castro, F.C. Gennari, J. Am. Ceram. Soc. 87 (2004) 2020.
[20] T. Fend, B. Hoffschmidt, R. Pitz-Paal, O. Reutter, P. Rietbrock, Energy 29 (2004) 823.
[21] T. Fend, R. Pitz-Paal, O. Reutter, J. Bauer, B. Hoffschmidt, Sol. Energy Mater. Sol. Cells 84 (2004) 291.
[22] B. Hoffschmidt, V. Fernández, A.G. Konstandopoulos, I. Mavroidis, M. Romero, P. Stobbe, F. Téllez, in: K.H. Funken, W. Bucher (Eds.), Proceedings of Fifth Cologne Solar Symposium, DLR, Germany, 2001, p. 51.
[23] C.C. Agrafiotis, I. Mavroidis, A.G. Konstandopoulos, B. Hoffschmidt, P. Stobbe, M. Romero, V. Fernandez-Quero, Sol. Energy Mater. Sol. Cells 91 (2007) 474.
[24] R.M. Heck, R.J. Farrauto, Catalytic Air Pollution Control-Commercial Technology, Van Nostrand Reinhold, New York, 1995.
[25] J.W. Geus, J.C. van Giezen, Catal. Today 47 (1999) 169.
[26] L. Nalbandian, V.T. Zaspalis, A. Evdou, C. Agrafiotis, A.G. Konstandopoulos, Chem. Eng. Trans. 4 (2004) 43.
[27] C. Agrafiotis, M. Roeb, A.G. Konstandopoulos, L. Nalbandian, V.T. Zaspalis, C. Sattler, P. Stobbe, A.M. Steele, Sol. Energy 79 (2005) 409.
[28] M. Roeb, C. Sattler, R. Klüser, N. Monnerie, L. de Oliveira, A.G. Konstandopoulos, C. Agrafiotis, V.T. Zaspalis, L. Nalbandian, P. Stobbe, A.M. Steele, J. Sol. Energy Eng. Trans. ASME 128 (2006) 125.
[29] C. Agrafiotis, C. Pagkoura, S. Lorentzou, J.C. Hoguet, A.G. Konstandopoulos, in: Proceedings of the 16th World Hydrogen Energy Conference, Lyon, France, 2006, pp. 13–16.
[30] M. Roeb, N. Monnerie, M. Schmitz, C. Sattler, A.G. Konstandopoulos, C. Agrafiotis, V.T. Zaspalis, L. Nalbandian, A. Steele, P. Stobbe, Poceedings of the 16th World Hydrogen Energy Conference, Lyon, France, 2006, pp. 13–16.
[31] C. Agrafiotis, S. Lorentzou, C. Pagkoura, M. Kostoglou, A.G. Konstandopoulos, in: Proceedings of SolarPACES 13th International Symposium on Concentrated Solar Power and Chemical Energy Technologies, Seville, Spain, 2006, pp. 20–23.
[32] S. Lorentzou, K. Karadimitra, C. Agrafiotis, A.G. Konstandopoulos, in: Proceedings of PARTEC 2004 International Conference for Particle Technology, Nuremberg, Germany, 2004, pp. 16–18.
[33] T. Kodama, Y. Kondoh, R. Yamamoto, H. Andou, N. Satou, Sol. Energy 78 (2005) 623.
[34] P. Koí, M. Marek, M. Kubíek, T. Maunula, M. Härkönen, Chem. Eng. J. 97 (2004) 131.
[35] S.T. Kolaczkowski, P. Crumpton, A. Spence, Chem. Eng. Sci. 43 (1988) 227.
[36] G. Gropi, E. Tronconi, AIChE J. 42 (1996) 2382.
[37] C. Dubien, D. Schweich, G. Mabilon, B. Martin, M. Prigent, Chem. Eng. Sci. 53 (1998) 471.
[38] J. Villadsen, M.L. Michelsen, Solution of Differential Equation Models by Polynomial Approximation, Prentice Hall, New York, 1978.